*Article*

# Effect of Mg Doping on the Physical Properties of Fe$_2$O$_3$ Thin Films for Photocatalytic Devices

**Rihab Ben Ayed** [1,2]**, Mejda Ajili** [1]**, Yolanda Piñeiro** [2]**, Badriyah Alhalaili** [3]**, José Rivas** [2]**, Ruxandra Vidu** [4,5,*]**, Salah Kouass** [6] **and Najoua Kamoun Turki** [1]

[1] LR99ES13 Laboratoire de Physique de la Matière Condensée (LPMC), Département de Physique, Faculté des Sciences de Tunis, Université Tunis El Manar, Tunis 2092, Tunisia; rihab.benayed@fst.utm.tn (R.B.A.); ajili.mejda@yahoo.fr (M.A.); n.najouakamoun@gmail.com (N.K.T.)

[2] Nanomag Laboratory, Applied Physics Department, Universidade de Santiago de Compostela, 15782 Santiago de Compostela, Spain; yolanda.fayoly@gmail.com (Y.P.); jose.rivas@usc.es (J.R.)

[3] Nanotechnology and Advanced Materials Program, Kuwait Institute for Scientific Research, P.O. Box 24885, Safat 13109, Kuwait; bhalalil@kisr.edu.kw

[4] Faculty of Materials Science and Engineering, University Politehnica of Bucharest, 060042 Bucharest, Romania

[5] Department of Electrical and Computer Engineering, University of California Davis, Davis, CA 95616, USA

[6] Laboratoire des Matériaux Utiles, INRAP, Technopôle, Sidi-Thabet, Tunis 2020, Tunisia; koissa2000@yahoo.fr

* Correspondence: rvidu@ucdavis.edu

**Abstract:** Undoped and Mg-doped (y = [Mg$^{2+}$]/[Fe$^{3+}$] = 1, 2, 3, and 4 at.%) Fe$_2$O$_3$ thin films were synthesized by a simple spray pyrolysis technique. The thin films were extensively characterized. X-ray diffraction (XRD) and energy-dispersive spectroscopy (EDS) analysis confirmed the successful insertion of Mg in the rhombohedral structure of Fe$_2$O$_3$. In addition, scanning electronic microscope (SEM) and confocal microscope (CM) images showed a homogenous texture of the film, which was free of defects. The rough surface of the film obtained by spray pyrolysis is an important feature for photocatalysis and gas sensor applications. The direct band gap of the doped Fe$_2$O$_3$ films obtained for [Mg$^{2+}$]/[Fe$^{3+}$] = 3 at.% was E$_{dir}$ = 2.20 eV, which recommends the Mg-doped iron oxide as an optical window or buffer layer in solar cell devices. The photodegradation performance of Mg-doped Fe$_2$O$_3$ was assessed by studying the removal of methylene blue (MB) under sunlight irradiation, with an effective removal efficiency of 90% within 180 min. The excellent photodegradation activity was attributed to the strong absorption of Mg-doped Fe$_2$O$_3$ in the UV and most of the visible light, and to the effective separation of photogenerated charge carriers.

**Keywords:** thin films; iron oxide; Mg doping; physical properties; photocatalysis

## 1. Introduction

Maintaining a clean environment has become an inspiring research ambition in the environmental-science-related communities. As a global environmental issue, water pollution threats our life. For example, eco-clean technology is urgently needed to deal with dyes that are manufactured, used, and thrown into the water. Photocatalysis draws attention to the need for extensive research and investigations into water purification and generation of renewable energies [1–4]. The oxide semiconductor photocatalyst has received special attention as a beneficial material with easy-to-control properties. The basic idea of photocatalysis is the activation of the semiconductor through an artificial or a natural source of light, which breaks down the organic compounds and dyes to purify water [3]. Ferric oxide (Fe$_2$O$_3$), as an environmental green oxide with outstanding physical and chemical properties, has been the subject of a great deal of research [5,6]. Fe$_2$O$_3$, as a mid-band gap semiconductor, utilizes sunlight effectively in the photocatalysis process as compared to TiO$_2$, which is the most researched photocatalyst [7–10]. Numerous methods were adopted to enhance the photocatalytic activity in metal oxide semiconductors, such as the

formation of junctions and doping to prevent the electron-hole ($e^-/h^+$) recombination and to enhance the photocatalysis process, where dopant ions act as charge traps, reducing the recombination of $e^-/h^+$ [11–13]. The photocatalytic degradation of rhodamine B (RhB) with sprayed $Fe_2O_3$ films under sunlight illumination was investigated. The efficiency of RhB decomposition was observed to be 73% during 400 min [14]. Jiamprasertboon et al. prepared an $\alpha$-/$Fe_2O_3$/ZnO and ZnO/$\alpha$-$Fe_2O_3$ heterojunction using aerosol-assisted chemical vapor deposition (AACVD). The $\alpha$-Fe2O3/ZnO exhibited the highest photocatalytic activity under UVA light, which was approximately 16 and 2.5 times higher than that of the Fe2O3 and ZnO layers. In contrast, the reverse heterojunction architecture was less active [15]. Furthermore, $Fe_2O_3$ and $Zn:Fe_2O_3$ nanoparticles were prepared via sol-gel with different Zn ratios. The photodegradation analysis of 4 at.% $Zn:Fe_2O_3$ showed 87% of RB dye degraded in 90 min in the UV light compared to 63% with pure $Fe_2O_3$, and a further increase in Zn content decreased the degradation efficiency [16]. Gajendra K. Pradhan et al. found that Pt-doping enhances the catalytic activity, where, via hydrothermal technique, Pt-doped hematite nanorod showed 63% decomposition of congo red and 55% efficiency towards methylene blue under 4 h of reaction in solar light compared to $Fe_2O_3$ [17]. Satheesh et al. elaborated undoped and doped $M:Fe_2O_3$ (M = Cu, Ni, and Co) using co-precipitation method, with the photocatalytic activity evaluated by the Acid Red-27 (AR-27) degradation under visible light irradiation. $Cu:Fe_2O_3$ showed the highest activity, with around 98.05% of AR-27 being degraded in 90 min, which was higher than that of $Fe_2O_3$ (77.68%), $Ni:Fe_2O_3$ (41.60%), and $Co:Fe_2O_3$ (59.67%) [18]. Nevertheless, an efficient dopant could significantly improve the activity of $Fe_2O_3$. Recently, J. A. Joseph et al. published a paper about Mg-doped iron oxide photocatalytic efficiency. Undoped and doped $Fe_2O_3$ nanostructures were grown by a two-stage electrochemical method. A Photocatalytic activity of 81% was obtained for the $Mg:Fe_2O_3$ nanostructures in 180 min, while $Fe_2O_3$ possessed only 56% of degradation. However, no reports are available on the sprayed Mg-doped hematite for MB degradation [19].

Undoped and doped $Fe_2O_3$ thin films are commonly fabricated by various chemical and physical techniques, such as sol-gel [20], chemical bath deposition [21], chemical spray pyrolysis [22], electrodeposition [23], and SILAR [24]. In addition, low-cost thin films can be deposited on different substrates by chemical spray pyrolysis for various industrial applications [25,26]. In this paper, the structural, morphological, elemental, and optical properties of Mg-doped $Fe_2O_3$ obtained by chemical spray pyrolysis technique are presented. The photocatalytic activity of Mg-doped $Fe_2O_3$ on the photodegradation of methylene blue under sunlight irradiation was investigated, which, to our knowledge, has not yet been studied in the literature.

## 2. Materials and Methods

### 2.1. Preparation of Undoped and Mg-Doped Fe₂O₃ Thin Films

Undoped and Mg-doped $Fe_2O_3$ thin films were grown on ordinary glass substrates through chemical spray pyrolysis technique (CSP). Before the deposition process, all the glass substrates were carefully cleaned via immersion in an ultrasonic bath. Iron III chloride ($FeCl_3$ and $6H_2O$) and ($MgCl_2$ and $6H_2O$) precursors were acquired from AppliChem (Council Bluffs, IA, USA). Both precursors was dissolved in 100 mL of bi-distilled water, where $MgCl_2$ was added as a dopant. The Mg ratio was adjusted at y = $[Mg^{2+}]/[Fe^{3+}]$ = 1, 2, 3, and 4 at.%. On the other hand, the iron chloride concentration was kept at 0.14 mol·$L^{-1}$. The as-prepared solutions were mixed until obtaining homogenous mixtures. The aqueous solution was sprayed with a flow rate equal to 5 mL·$min^{-1}$ by means of compressed air on preheated substrates located 25 cm from the nozzle at 400 °C for 20 min.

### 2.2. Photocatalytic Activity

The photocatalytic activity was assessed by evaluating the degradation of methylene blue (MB) solution under sunlight illumination. The Mg-doped $Fe_2O_3$ film was immersed in 50 mL aqueous MB solution with a concentration of 5 mg/mL and kept under sunlight

irradiation for various times (0–180 min). The photodegradation of MB was then estimated by the maximum absorbance at a wave length of 664 nm using Vis-spectrophotometer (Perkin Elmer Lambda 950). According to the Beer–Lambert law, the degradation efficiency of methyl blue was computed starting from the absorbance spectra using the following equation [27]:

$$\text{Degradation Efficiency (\%)} = \frac{(A_0 - A)}{A_0} \times 100 \tag{1}$$

where $A_0$ and $A$ are the values of MB solution absorbance at reaction times of 0 and t, respectively.

The reaction kinetic was estimated using the following formula [27]:

$$\text{Ln}\left(\frac{A}{A_0}\right) = -kt \tag{2}$$

*2.3. Characterization*

All the samples were characterized by several techniques as discussed below. The crystalline quality of $Fe_2O_3$ thin layers was characterized by X-ray diffraction (XRD) using X-ray "XPERT-PRO" diffractometer (Malvern Panalytical Ltd., Malvern, UK) with CuKα ($\lambda$ = 1.54 Å) radiation over a scanning angle (2θ) ranging continuously from 25° to 60°. The experimental XRD spectra were refined with the MAUD software. The surface morphologies and cross-section of the thin films were observed using scanning electronic microscope (SEM) "ZEISS" (Carl Zeiss Microscopy, New York, USA) in surface (1 μm (EHT = 3.00 kV; Mag = 20.00 K) and 200 nm (EHT = 3.00 kV; Mag = 100.00 K)) and cross-section. In addition, 3D characterization was performed using a confocal microscope (CM) (SENSOFAR, Barcelona, Spain). The elemental composition was analyzed using energy-dispersive X-ray spectroscopy (EDS) "ZEISS". The optical measurements were carried out using a spectrophotometer, Perkin Elmer Lambda 950 (Bridgeport, CT, USA), over the wavelength range of 250–2000 nm.

## 3. Results and Discussion

*3.1. Structural Properties*

The influence of Mg-doping on the crystalline structure of the as-synthesized iron oxide composites was examined by X-ray diffraction. As shown in Figure 1, six diffraction peaks located at 2θ = 24.23, 33.24, 35.75, 44.99, 49.56, and 54.18° can be observed in the XRD patterns of the undoped and Mg-doped $Fe_2O_3$ thin films, corresponding to the (012), (104), (110), (113), (024), and (116) planes, respectively, of a typical $\alpha$-$Fe_2O_3$ phase structure (rhombohedral, R-3C, a = b = 5.023 Å, c = 13.70 Å; JCPDS Card No. 01-089-8104) [28,29]. No new peak formation was observed, which confirms that magnesium has been successfully substituted into the $Fe_2O_3$ matrix. The X-ray analysis shows that all films are polycrystalline and have a preferential orientation along the (104) plane, regardless of the Mg doping level. A slight shift to higher diffraction angles was detected in the XRD scans of the doped samples, especially for 1 at.% and 2 at.%. The shift was attributed to the seamless incorporation of magnesium ions into the $Fe_2O_3$ structure, due to the smaller ionic radius of $Mg^{2+}$ compared to $Fe^{3+}$ [30,31]. We note that the highest intensity of the principal orientation was obtained at 3 at.% Mg doping concentration.
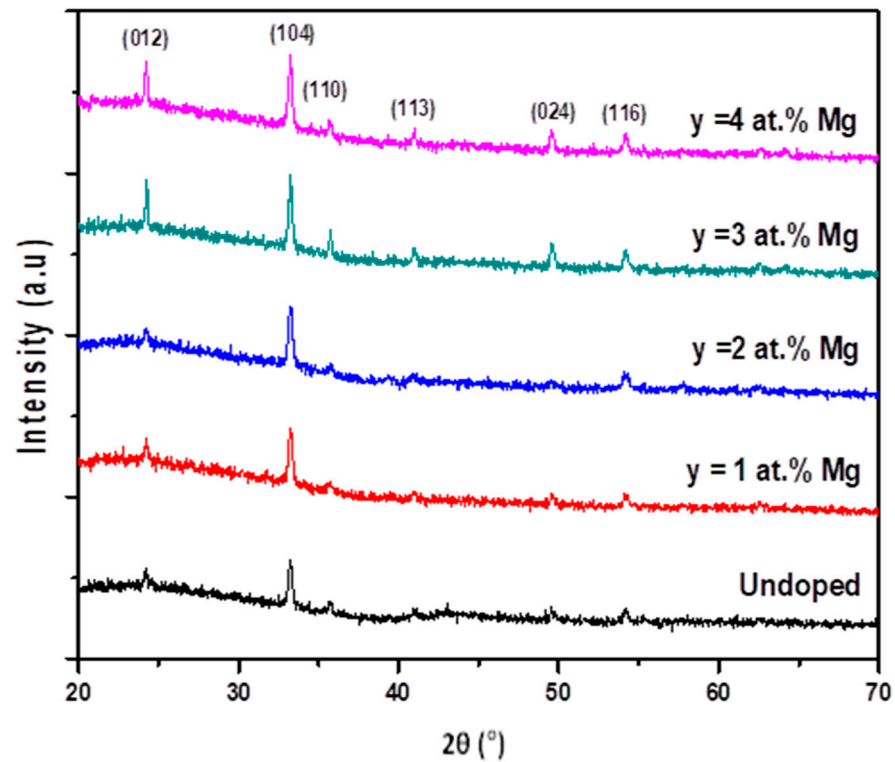
**Figure 1.** XRD patterns of undoped and Mg-doped $Fe_2O_3$ thin films for different contents (y = $[Mg^{2+}]/[Fe^{3+}]$ = 1, 2, 3, and 4 at.%).

The preferred orientation degree (Tc) in the (hkl) orientation was determined using the following empirical relation [27]:

$$T_{C_{(hkl)}} = \frac{I_{(hkl)}/I_{0(hkl)}}{\frac{1}{N}\sum_N \left(\frac{I_{(hkl)}}{I_{0(hkl)}}\right)} \tag{3}$$

where (hkl) are the Miller indices, $I_0$ is the standard intensity, I is the measured intensity, and N is the number of reflection peaks. The variation of the Tc (104) and Tc (110) values with the doping concentration of Mg is represented in Figure 2, which shows that the tendency of crystallites to develop along the (110) plane increases with the increase of the Mg doping concentration up to 3 at.%. Although (104) is the major orientation, the variation of the intensity of the (110) plane, which presents a random orientation of crystallite, confirms the polycrystalline character of the Mg-doped thin films.

The lattice constants a and c of the nanocrystals and the cell volume of all the samples were estimated according to the following equations [7]:

$$\frac{1}{d_{hkl}^2} = \frac{4}{3a^2}\left(h^2 + k^2 + hk\right) + \frac{l^2}{c^2} \tag{4}$$

$$V = \frac{\sqrt{3}}{2}a^2c \tag{5}$$

where $d_{hkl}$ is the interplanar distance. The estimated values of lattice parameter are presented in Table 1. The calculated values of the unit cell parameters of Mg-doped $Fe_2O_3$ were found to be lower than those of the undoped films, which result in a decrease in the cell volume. Magnesium incorporation caused local changes in the $Fe_2O_3$ matrix, which confirms the successful fabrication of Mg-doped $Fe_2O_3$ thin film [32–34]. For further

investigation of the impact of Mg doping on the film microstructure, the average crystallite size and macrostrain of the films were estimated using Williamson–Hall formula [22]:

$$\frac{\beta \cos \theta}{\lambda} = \frac{1}{D} + \varepsilon \frac{\sin \theta}{\lambda} \tag{6}$$

where $\beta$ is FWHM in radian, D is the grain size in nanometers, $\varepsilon$ is the microstrain, and $\lambda$ is X-ray wavelength in nanometers. The values estimated from Figure 3 are presented in Table 1, which shows that D decreased from 60.8 nm to 55.3 nm regardless of the doping concentration. Consequently, the microstrain increased from $0.31 \times 10^{-3}$ to $0.64 \times 10^{-3}$. The decrease in the lattice parameters (a,c) and cell volume (V) presented in Table 1 is expected due to the stoichiometric replacement of Fe ions with Mg ions with smaller ionic radii. The smallest volume, V, was obtained for y = 3 at.%, corresponding to the best crystalline quality (Figures 1 and 2), which is also in agreement with the substitution of Fe by Mg in the lattice [33].
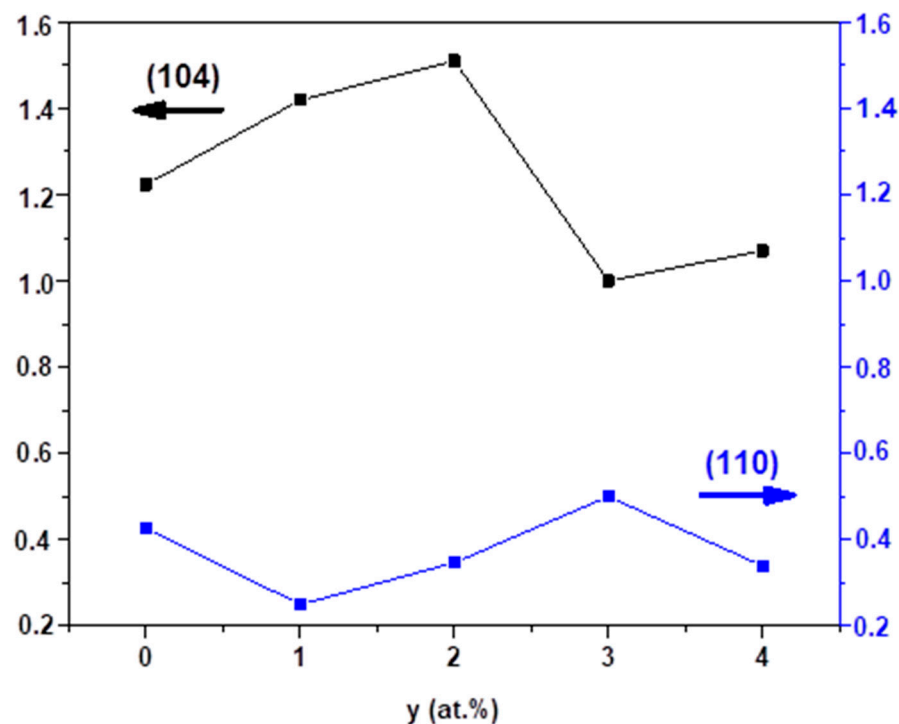


**Figure 2.** Texture coefficient ($T_C$) for (104) and (110) directions in undoped and Mg-doped $Fe_2O_3$ grown films ($0 \leq y = [Mg^{2+}]/[Fe^{3+}] \leq 4$ at.%).

**Table 1.** The variation of grain size (D), microstrain ($\varepsilon$), and lattice parameters (a and c) and unit cell volume (V) versus Mg (at.%) content.

| Mg (at.%) | D (nm) | $\varepsilon \times 10^{-3}$ | a (Å) | c (Å) | V (Å³) |
|---|---|---|---|---|---|
| 0 | 60.8 | 0.31 | 5.034 | 13.77 | 302.18 |
| 1 | 59.2 | 0.53 | 5.026 | 13.74 | 300.57 |
| 2 | 57.7 | 0.55 | 5.024 | 13.73 | 300.11 |
| 3 | 55.3 | 0.62 | 5.022 | 13.72 | 299.65 |
| 4 | 55.9 | 0.64 | 5.024 | 13.72 | 299.89 |
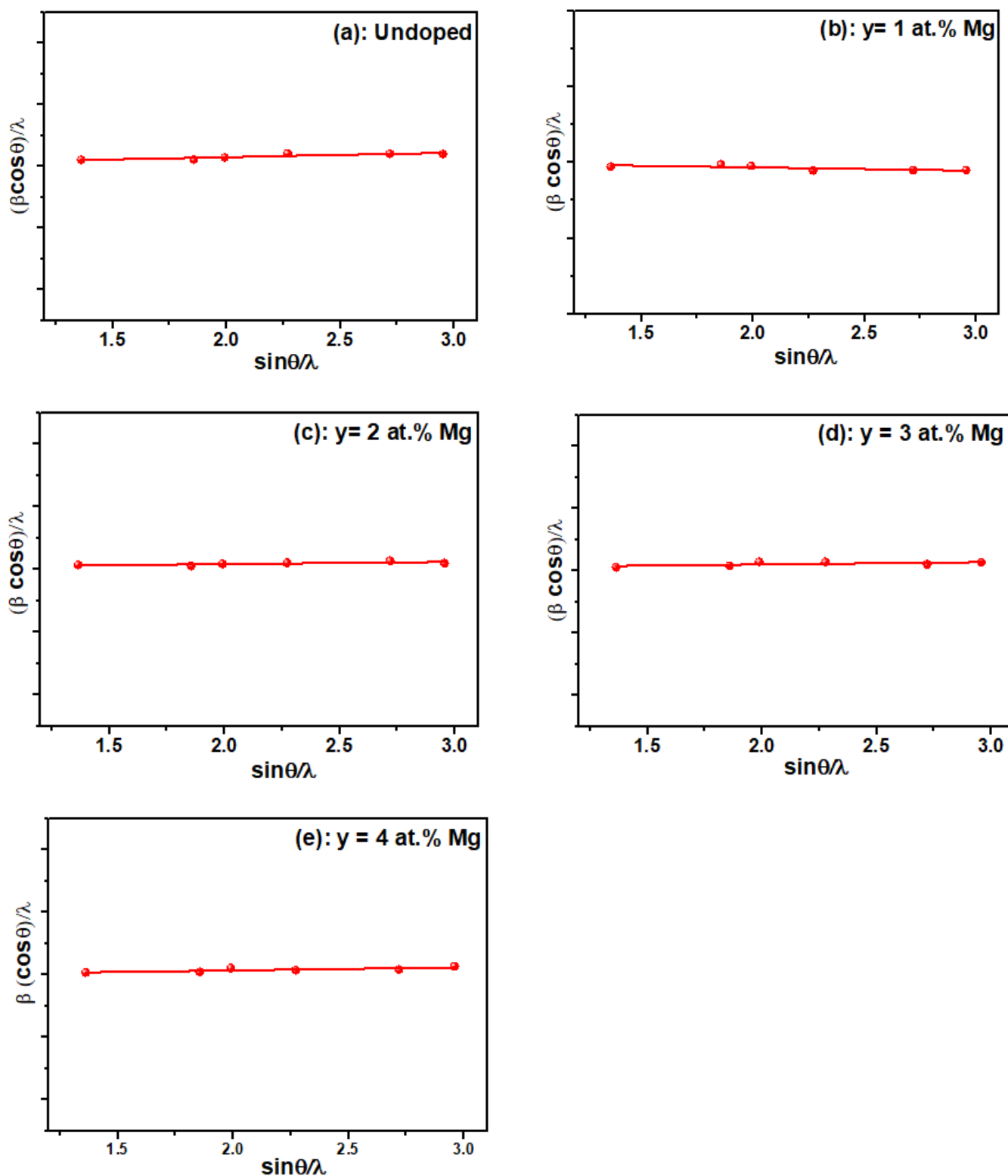
**Figure 3.** Williamson–Hall plots for the undoped and Mg-doped $Fe_2O_3$ thin films.

### 3.2. Rietveld Analysis

Rietveld analysis (using MAUD software) was used for the 3 at.% Mg-doped $Fe_2O_3$ thin films to check the $\alpha$-$Fe_2O_3$ phase purity. The refinement plot is shown in Figure 4, which represents the experimental pattern as black dots and the pattern calculated with Rietveld refinement as red solid lines. In addition, the lower part of the graph indicates the difference between the values of experimental and calculated intensities. The structural

fitting quality was checked by the goodness-of-fit factor (GoF = Rwp/Rexp), where Rwp is the weighted residual error and Rexp is the expected error. The GoF was found to be 1.26, which describes a well-fitting model with low discrepancies between the experimental and calculated XRD patterns [7,35]. The results obtained confirm that the Fe ion was substituted by the Mg ion in the $Fe_2O_3$ phase.
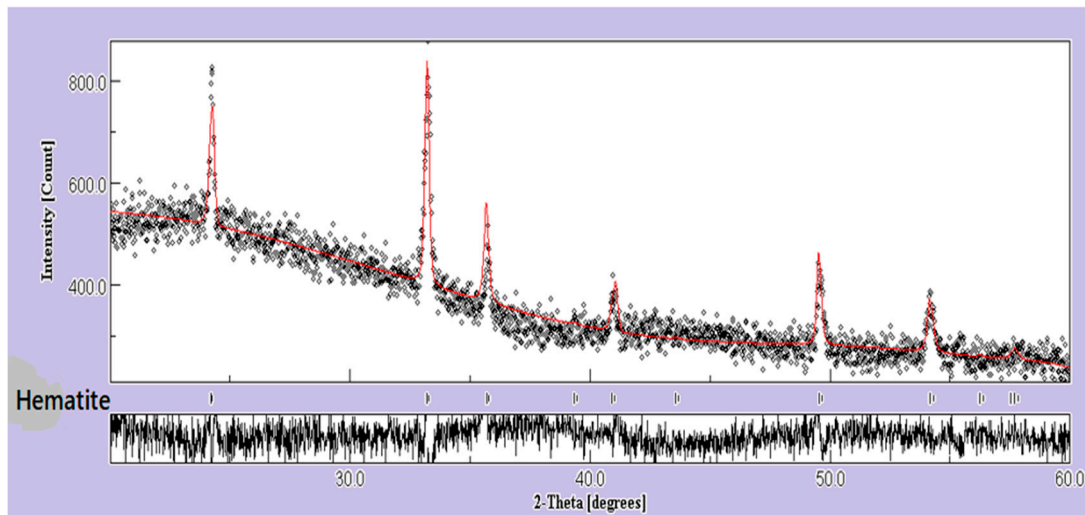


**Figure 4.** Rietveld refinement patterns of 3 at.% Mg-doped $Fe_2O_3$ samples (dots for experimental and solid line for simulated curves).

### 3.3. Morphological Properties

The effect of magnesium doping on the morphology of $Fe_2O_3$ films is shown in Figure 5a–e. The SEM micrographs show a granular morphology with a uniform distribution through the substrate surface for the undoped and doped samples. A similar morphology was mentioned in literature [5,22,28]. The cross-section images show a compact and homogenous textured film with a thickness of about 384 and 340 nm for undoped $Fe_2O_3$ and 3 at.% Mg-doped $Fe_2O_3$, respectively (Figure 5a,d). No defects are observed on the samples surface. The undoped films appear to have a randomly distributed grain agglomeration on the surface of the film. The Mg-doped films show a more uniform distribution with smaller grain size compared to the undoped films, which recommends them for photocatalysis applications [36]. At a higher Mg-doping concentration, the rhombohedral shape of the grains appears more clearly defined (inset Figure 5d,e).

In order to better understand the effect of Mg doping on the morphological properties of the $Fe_2O_3$ thin films, the topography evolution of the deposited films was investigated using confocal microscope (CM). Figure 6 presents the 3D CM images of the thin films. Overall, these images are in agreement with those observed by SEM (Figure 5). The 3D micrographs show a homogenous layer free from voids and cracks. The surface roughness parameters, including the root mean square (Sq) and arithmetic average of absolute values (Sa), were extracted from CM data. The values of surface roughness of undoped and Mg-doped $Fe_2O_3$ thin films as a function of Mg concentrations are given at Table 2. The Sa and Sq values vary in the range [60.6–76.6] nm and [80.6–104.1] nm, respectively. Mg-doped $Fe_2O_3$ layers have a relatively high surface roughness, which can offer more available active sites and, consequently, improve the adsorption of pollutants during the photocatalysis process [18]. The highest values of Sa and Sq were obtained for a Mg content of 3 at.% (Table 2).
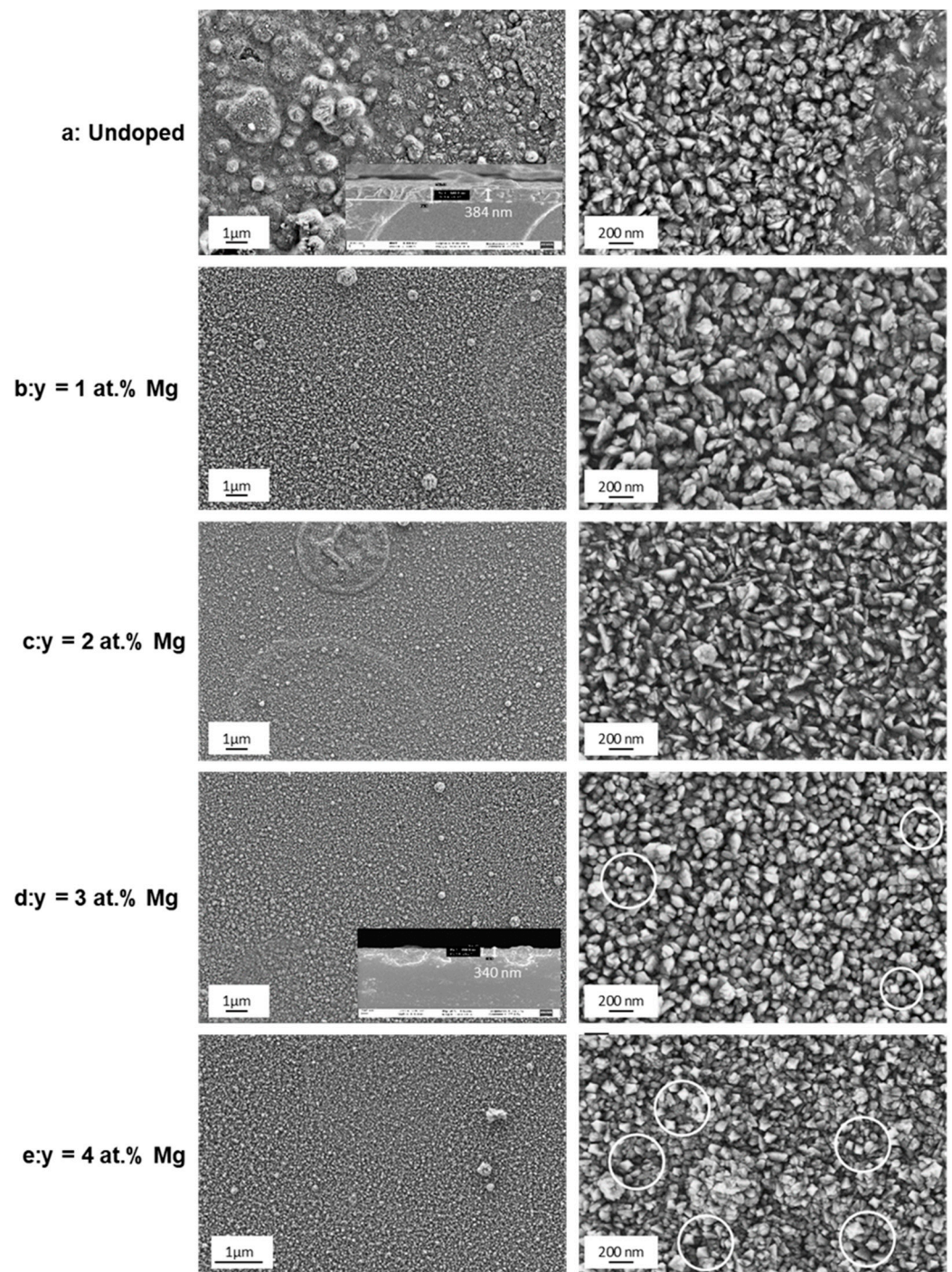
**Figure 5.** SEM images at two magnifications (1 μm and 200 nm) of the undoped and Mg-doped $Fe_2O_3$. The inlets show the cross-sections of the respective thin films.
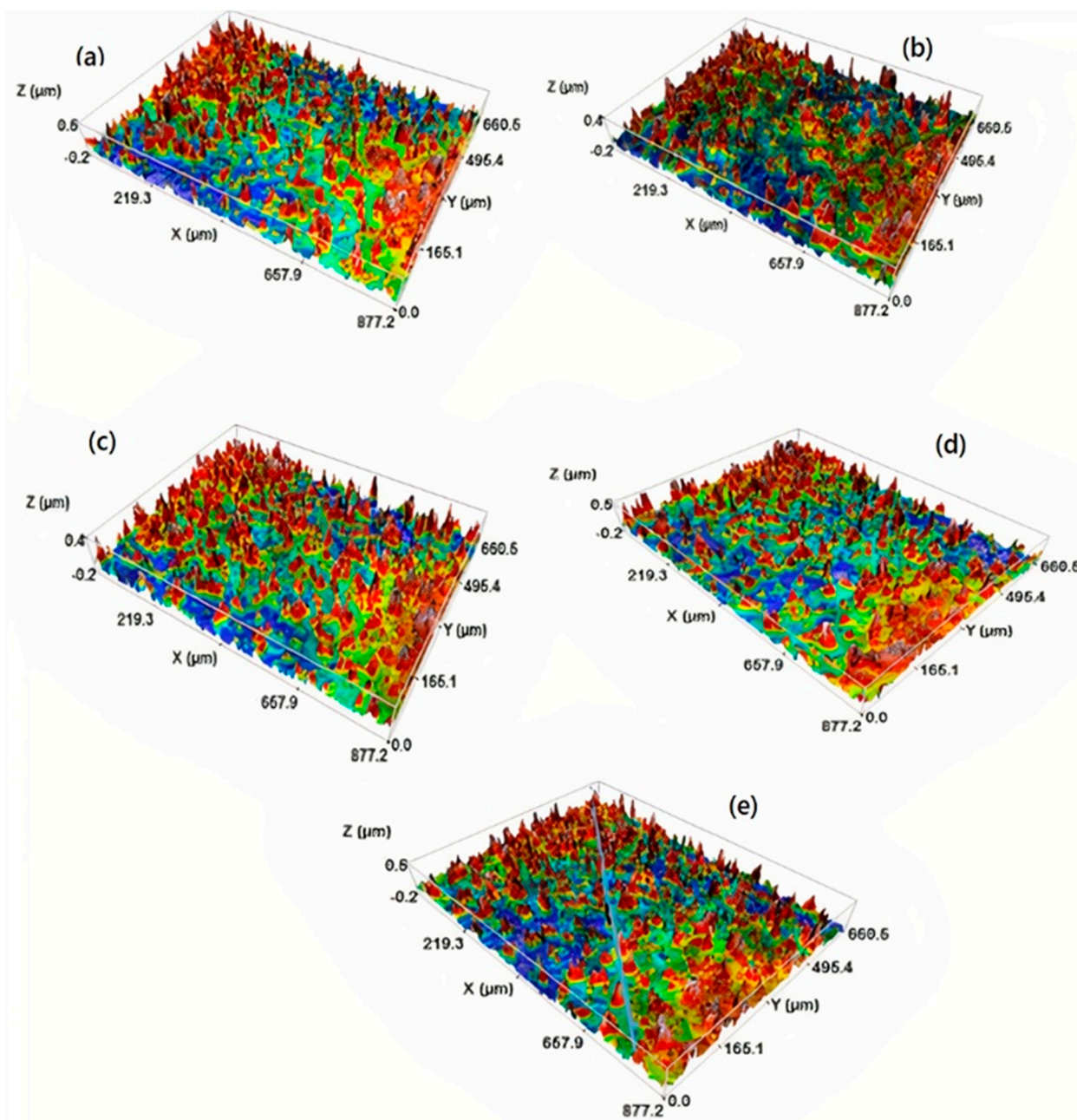
**Figure 6.** 3D CM micrographs of undoped and Mg-doped $Fe_2O_3$ with different contents ((**a**) undoped, (**b**) 1 at.%, (**c**) 2 at.%, (**d**) 3 at.%, and (**e**) 4 at.%).

**Table 2.** The surface arithmetic average of absolute values ($S_a$) and root mean square ($S_q$) values for undoped and Mg-doped $Fe_2O_3$ thin films.

| Mg (at.%) | $S_a$ (nm) | $S_q$ (nm) |
|-----------|-----------|-----------|
| 0 | 70.7 | 95.1 |
| 1 | 63.4 | 85.5 |
| 2 | 60.6 | 80.6 |
| 3 | 76.6 | 104.1 |
| 4 | 74.9 | 102.6 |

The EDS spectra of the glass substrate and 3 at.% Mg-doped $Fe_2O_3$ film shown in Figure 7 reveal many peaks. The EDS analysis confirmed the presence of the expected

elements, iron (Fe), magnesium (Mg), and oxygen (O), all in addition to those attributed to glass substrate, confirming the grown layer free from impurities.
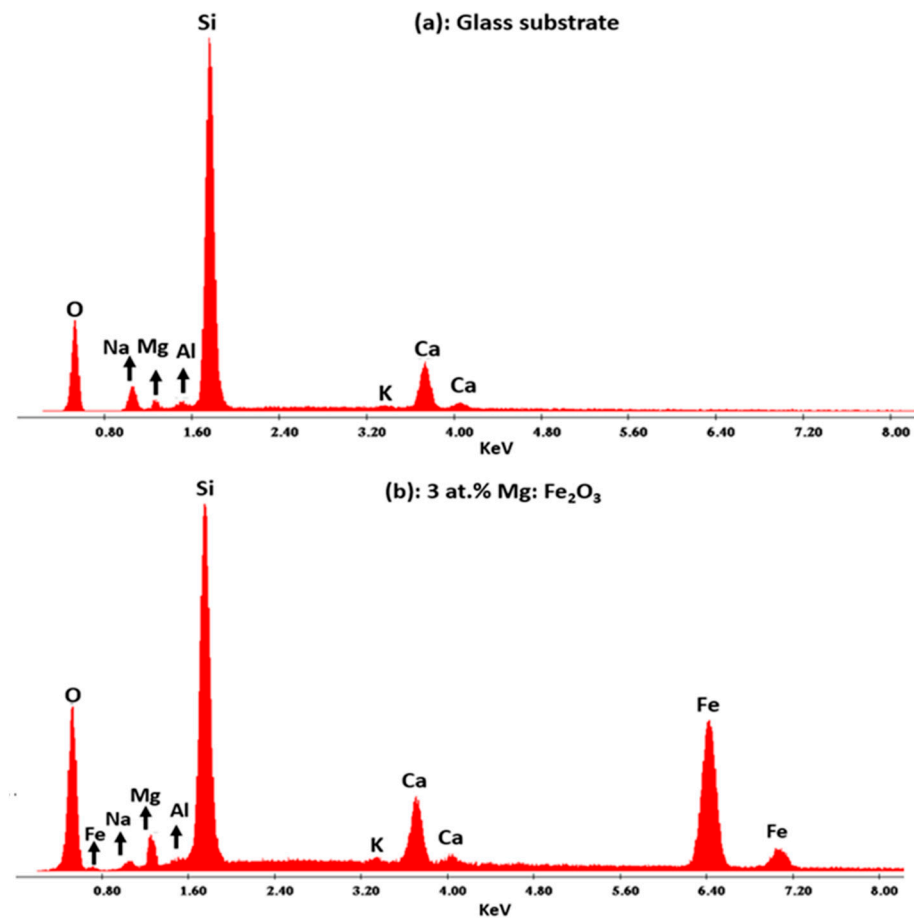


**Figure 7.** EDS Spectrum of the glass substrate (**a**) and 3 at.% Mg-doped $Fe_2O_3$ film (**b**).

*3.4. Optical Properties*

To investigate the doping effect of Mg (y = 1, 2, 3, and 4 at.%) on the optical properties of $Fe_2O_3$ thin films, transmission (T($\lambda$)) and reflection (R($\lambda$)) measurements were carried out. The T ($\lambda$) and R($\lambda$) spectra are presented in Figure 8, which shows that the as-deposited films have a high transmission coefficient ($\geq$60%) within the interval of 1000–2500 nm. Below 650 nm, a sharp fall in all the R–T spectra is observed, which is due to the very strong absorption of these films in the UV and most of the visible light region. Remarkably, in the SEM cross- section images (Figure 5), interference fringes are observed in the transmission spectra, referring to the films excellent thickness homogeneity [22,28]. The optical reflection data allow the estimation of the band gap values through the differential reflectance spectra (dR/d$\lambda$) as a function of wavelength. The optical direct (Edir) and indirect (Eind) band gaps values obtained for $Fe_2O_3$ and Mg-doped iron oxide semiconductor are typical of those for $Fe_2O_3$ (Table 3) [7]. No significant variation was observed for indirect transition ($E_{ind}$), but a slight increase of the direct transition value ($E_{dir}$) with Mg doping content was observed from 2.15 eV for $Fe_2O_3$ to 2.20 eV for 3 at.% Mg-doped $Fe_2O_3$ (Table 3). We observed that the films crystallinity improved with the Mg insertion (Figure 1). In addition, a slight increase in the direct band gap was noticed, to reach a maximum value equal to 0.05 eV with a magnesium doping ratio equal to 3 at.%. This finding is in good correlation with the crystallinity observed at the same doping ratio, which reduced the structural defects.
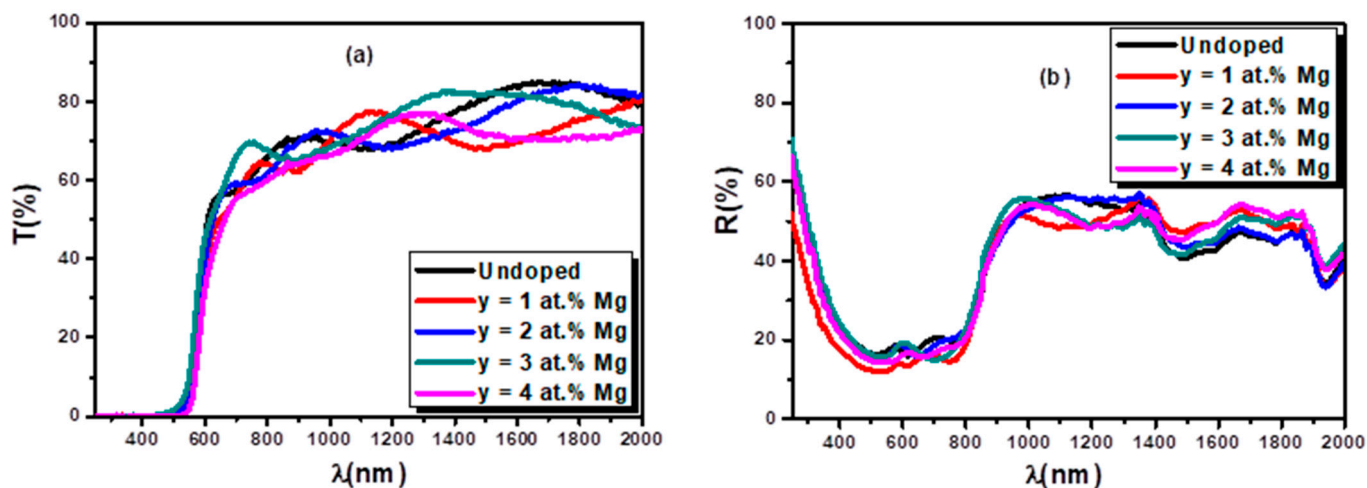
**Figure 8.** The optical transmittance (T) (**a**) and reflectance (R) (**b**) of undoped and Mg-doped $Fe_2O_3$.

**Table 3.** Direct ($E_{ind}$) and indirect ($E_{dir}$) band gaps energies values of undoped and Mg-doped $Fe_2O_3$ thin films.

| Mg (at.%) | $E_{dir}$ | $E_{ind}$ |
|:---:|:---:|:---:|
| 0 | 2.15 | 1.97 |
| 1 | 2.16 | 1.96 |
| 2 | 2.18 | 1.96 |
| 3 | 2.20 | 1.99 |
| 4 | 2.16 | 1.97 |

*3.5. Photocatalytic Activity*

It is well recognized that the photocatalysis process occurs through the photogeneration of electron-hole pairs under light irradiation [2,4]. When photons reach a semiconductor catalyst, an electron absorbs the photon energy to move from valence band to occupy conduction band levels, leaving behind an electron vacancy (hole); thus, creating the electron-hole pairs. On the other hand, the lifetime of electron-hole pairs is very short [13,15,17]. To ensure the conservation of the charges, that is when the electron and/or hole is filled by an arbitrary charge, and the photocatalytic reaction may take place. In order to study the photocatalytic activity of Mg-doped $Fe_2O_3$ thin films, many parameters such as adsorption process, particle size, morphology, and crystallinity catalyst performance were considered. Mg-doped $Fe_2O_3$ with y = 3 at.% provides a good platform for the photodegradation of organic dyes. Figure 9a shows the absorbance spectra recorded in the wavelength range from 400 to 800 nm. As shown in the absorption spectra of MB, the main peak intensity occurred at 664 nm over the reaction time using Mg-doped $Fe_2O_3$ as catalyst. As irradiation was carried out, the absorption intensity decreased, with about 90% of degradation achieved within 180 min (Figure 9b) This film shows higher degradation efficiency compared with the undoped $Fe_2O_3$ thin films, which degraded almost 50% of MB under (Figure 9a) sunlight irradiation. The substitution of $Fe^{3+}$ by $Mg^{2+}$ sited onto the $Fe_2O_3$ lattice led to the enhancement in the photocatalytic activity. The possible reaction mechanism for the photocatalytic process of the mentioned sample is shown below [12]:

$$Mg{:}Fe_2O_3 + h\nu \rightarrow Mg{:}Fe_2O_3 \ (e^- + h^+) \tag{7}$$

$$e^-_{BC} + O_2 \rightarrow O_2^\circ \tag{8}$$

$$h^+_{BV} + H_2O \rightarrow OH^\circ + H^+ \tag{9}$$

$$MB + (OH^\circ, O_2^{\circ-}) \rightarrow Intermediates \rightarrow Decomposition \ product \tag{10}$$
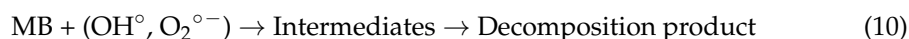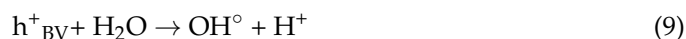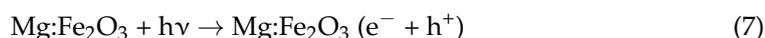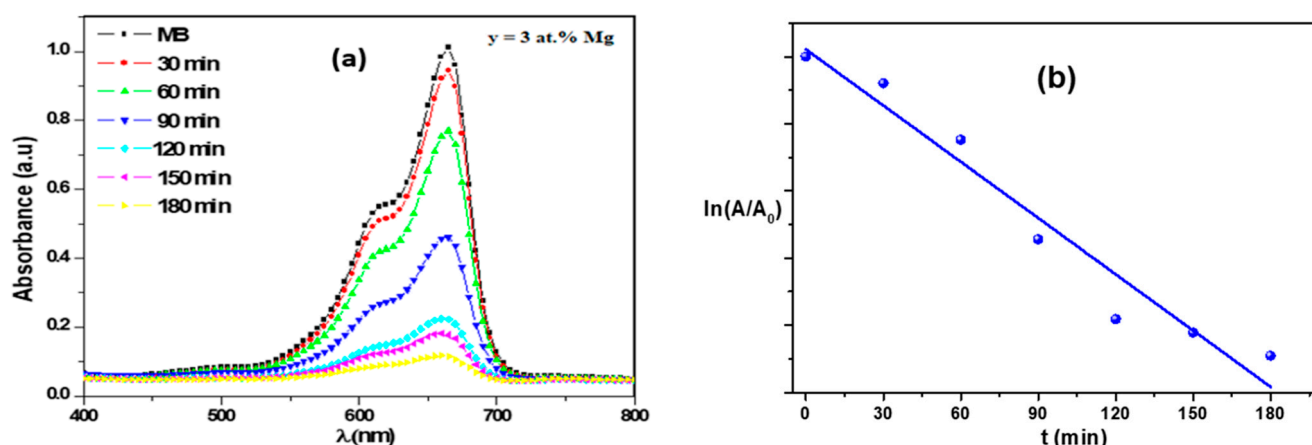
**Figure 9.** Time-dependent absorption spectra of MB dye solution in the presence of $Fe_2O_3$ (**a**), 3 at.% Mg-doped $Fe_2O_3$ (**b**) and kinetic degradation of MB dye.

As a result, the linked works of the photogenerated electrons and holes cause the MB degradation, where the e- reacts with oxygen molecules to produce superoxide anion radicals ($O_2^{\circ-}$) and the $h^+$ reacts with water to form hydroxyl radicals. The inserted magnesium ions act like a charge sink, which consequently can enhance the separation of the photogenerated charge pairs, giving rise to further superoxide and hydroxyl radicals, leading to an enhancement in the photocatalytic degradation efficiency. Many researchers have reported that the activity of semiconductor materials in dye degradation processes is affected by metal transition dopants [13,17,18]. In order to investigate the kinetic of MB photodecomposition on the catalyst surface, Figure 9b shows the curve fitting of the kinetic equation. A straight line was obtained, indicating that the reaction is of pseudo-first order. Thus, 3 at.% Mg-doped $Fe_2O_3$ thin layer presents a performant photocatalyst.

## 4. Conclusions

$Fe_2O_3$ and Mg-doped $Fe_2O_3$ films were grown using chemical spray pyrolysis technique and then characterized using several analytical techniques. A structural characterization study revealed that all the films are highly crystallized in the rhombohedral structure with (104) as principal orientation, which confirms that Mg was well-incorporation onto the $Fe_2O_3$ lattice, especially for 3 at.% of Mg-doped $Fe_2O_3$. The morphological properties of the films showed a rough surface with granular texture, with the highest values of Sa and Sq for 3 at.% Mg-doped $Fe_2O_3$. Moreover, the roughness values obtained for 3 at.% Mg-doped $Fe_2O_3$ may improve the sensitivity of iron oxide to detect toxic gases, which recommends the 3 at.% Mg-doped Fe2O3 thin film for gas sensor devices. The Mg doping did not significantly affect the indirect optical band gap (Eind), while the direct band gap increased from 2.15 eV for undoped films to 2.20 eV for 3 at.% Mg-doped $Fe_2O_3$. These band gaps values of Mg-doped $Fe_2O_3$ recommend the use of these films as an optical window or buffer layer in photovoltaic devices. Otherwise, magnesium incorporation enhanced the photogenerated charge separation, greatly improving the photocatalytic performance of iron oxide material. The dye degradation activity of the 3 at.% Mg-doped $Fe_2O_3$ catalyst reached 90% after 180 min of sunlight irradiation.

**Author Contributions:** Conceptualization, N.K.T.; formal analysis, M.A., Y.P., B.A., J.R., R.V., S.K. and N.K.T.; investigation, R.B.A., M.A. and B.A.; methodology, R.B.A. and B.A.; resources, R.V.; supervision, N.K.T.; validation, Y.P., J.R., R.V. and N.K.T.; writing—original draft, R.B.A. All authors have read and agreed to the published version of the manuscript.

**Data Availability Statement:** The data is available on reasonable request from the corresponding author.

**Conflicts of Interest:** The authors declare no conflict of interest.

## References

1. Belver, C.; Bedia, J.; Gómez-Avilés, A.; Peñas-Garzón, M.; Rodriguez, J.J. Chapter 22—Semiconductor Photocatalysis for Water Purification. In *Nanoscale Materials in Water Purification*; Thomas, S., Pasquini, D., Leu, S.-Y., Gopakumar, D.A., Eds.; Elsevier: Amsterdam, The Netherlands, 2019; pp. 581–651.
2. Dias, E.M.; Petit, C. Towards the Use of Metal–Organic Frameworks for Water Reuse: A Review of the Recent Advances in the Field of Organic Pollutants Removal and Degradation and the Next Steps in the Field. *J. Mater. Chem. A* **2015**, *3*, 22484–22506. [CrossRef]
3. Li, Y.; Chen, F.; He, R.; Wang, Y.; Tang, N. Chapter 24–Semiconductor Photocatalysis for Water Purification. In *Nanoscale Materials in Water Purification*; Thomas, S., Pasquini, D., Leu, S.-Y., Gopakumar, D.A., Eds.; Elsevier: Amsterdam, The Netherlands, 2019; pp. 689–705.
4. Zargazi, M.; Entezari, M.H. Anodic Electrophoretic Deposition of Bi2WO6 Thin Film: High Photocatalytic Activity for Degradation of a Binary Mixture. *Appl. Catal. Environ.* **2019**, *242*, 507–517. [CrossRef]
5. Barroso, M.; Cowan, A.J.; Pendlebury, S.R.; Grätzel, M.; Klug, D.R.; Durrant, J.R. The Role of Cobalt Phosphate in Enhancing the Photocatalytic Activity of $\alpha$-Fe$_2$O$_3$ Toward Water Oxidation. *J. Am. Chem. Soc.* **2011**, *133*, 14868–14871. [CrossRef] [PubMed]
6. Mishra, M.; Chun, D.-M. A-Fe$_2$O$_3$ as a Photocatalytic Material: A Review. *Appl. Catal. Gen.* **2015**, *498*, 126–141. [CrossRef]
7. Ben Ayed, R.; Ajili, M.; Turki, N.K. Physical Properties and Rietveld Analysis of Fe$_2$O$_3$ Thin Films Prepared by Spray Pyrolysis: Effect of Precursor Concentration. *Phys. B Condens. Matter* **2019**, *563*, 30–35. [CrossRef]
8. Cesar, I.; Kay, A.; Gonzalez Martinez, J.A.; Grätzel, M. Translucent Thin Film Fe$_2$O$_3$ Photoanodes for Efficient Water Splitting by Sunlight: Nanostructure-Directing Effect of Si-Doping. *J. Am. Chem. Soc.* **2006**, *128*, 4582–4583. [CrossRef]
9. Liu, H.Y.; Shon, H.K.; Sun, X.; Vigneswaran, S.; Nan, H. Preparation and Characterization of Visible Light Responsive Fe$_2$O$_3$-TiO$_2$ Composites. *Appl. Surf. Sci.* **2011**, *257*, 5813–5819. [CrossRef]
10. Ounnar, A.; Bouzaza, A.; Favier, L.; Bentahar, F. Macrolide Antibiotics Removal Using a Circulating TiO$_2$-Coated Paper Photoreactor: Parametric Study and Hydrodynamic Flow Characterization. *Water Sci. Technol.* **2016**, *73*, 2627–2637. [CrossRef]
11. Baradaran, M.; Ghodsi, F.E.; Bittencourt, C.; Llobet, E. The Role of al Concentration on Improving the Photocatalytic Performance of Nanostructured ZnO/ZnO:Al/ZnO Multilayer Thin Films. *J. Alloys Compd.* **2019**, *788*, 289–301. [CrossRef]
12. Ali, D.; Butt, M.Z.; Muneer, I.; Farrukh, M.A.; Aftab, M.; Saleem, M.; Bashir, F.; Khan, A.U. Synthesis and Characterization of Sol-Gel Derived La and Sm Doped ZnO Thin Films: A Solar Light Photo Catalyst for Methylene Blue. *Thin Solid Film.* **2019**, *679*, 86–98. [CrossRef]
13. Xu, L.; Zheng, G.; Xian, F.; Su, J. The Morphological Evolution of ZnO Thin Films by Sn Ions Doping and Its Influence on the Surface Energy and Photocatalytic Activity. *Mater. Chem. Phys.* **2019**, *229*, 215–225. [CrossRef]
14. Mahadik, M.; Shinde, S.; Mohite, V.; Kumbhar, S.; Rajpure, K.; Annasaheb Moholkar, A.; Kim, J.; Bhosale, C. Photoelectrocatalytic Oxidation of Rhodamine B with Sprayed $\alpha$-Fe$_2$O$_3$ Photocatalyst. *Mater. Express* **2013**, *3*, 247–255. [CrossRef]
15. Jiamprasertboon, A.; Kafizas, A.; Sachs, M.; Ling, M.; Alotaibi, A.M.; Lu, Y.; Siritanon, T.; Parkin, I.P.; Carmalt, C.J. Heterojunction $\alpha$-Fe$_2$O$_3$/ZnO Films with Enhanced Photocatalytic Properties Grown by Aerosol-Assisted Chemical Vapour Deposition. *Chem. Eur. J.* **2019**, *25*, 11337–11345. [PubMed]
16. Sumna, S.; Chahal, S.; Kumar, A.; Kumar, P. Zn Doped $\alpha$-Fe$_2$O$_3$: An Efficient Material for UV Driven Photocatalysis and Electrical Conductivity. *Crystals* **2020**, *10*, 273. [CrossRef]
17. Pradhan, G.K.; Parida, K.M. Fabrication, Growth Mechanism, and Characterization of $\alpha$-Fe$_2$O$_3$ Nanorods. *ACS Appl. Mater. Interfaces* **2011**, *3*, 317–323. [CrossRef]
18. Satheesh, R.; Vignesh, K.; Suganthi, A.; Rajarajan, M. Visible Light Responsive Photocatalytic Applications of Transition Metal (M = Cu, Ni and Co) Doped $\alpha$-Fe$_2$O$_3$ Nanoparticles. *Biochem. Pharmacol.* **2014**, *2*, 1956–1968.
19. Joseph, J.A.; Nair, S.B.; Mary, S.A.; John, S.S.; Shaji, S.; Philip, R.R. Influence of Magnesium Doping on the Photocatalytic and Antibacterial Properties of Hematite Nanostructures. *Phys. Status Solidi* **2021**, *259*, 2100437. [CrossRef]
20. Watanabe, A.; Kozuka, H. Photoanodic Properties of Sol−Gel-Derived Fe$_2$O$_3$ Thin Films Containing Dispersed Gold and Silver Particles. *J. Phys. Chem. B* **2003**, *107*, 12713–12720. [CrossRef]
21. Cao, C.; Hu, C.; Shen, W.; Wang, S.; Song, S.; Wang, M. Improving Photoelectrochemical Performance by Building Fe$_2$O$_3$ Heterostructure on TiO$_2$ Nanorod Arrays. *Mater. Res. Bull.* **2015**, *70*, 155–162. [CrossRef]
22. Ayed, B.R.; Ajili, M.; Garcia, J.M.; Labidi, A.; Turki, N.K. Physical Properties Investigation and Gas Sensing Mechanism of Al: Fe$_2$O$_3$ Thin Films Deposited by Spray Pyrolysis. *Superlattices Microstruct.* **2019**, *129*, 91–104. [CrossRef]
23. Peeva, A.; Dikovska, A.O.; Atanasov, P.A.; de Castro, M.J.; Skorupa, W. Rare-Earth Implanted Y$_2$O$_3$ Thin Films. *Appl. Surf. Sci.* **2007**, *253*, 8165–8168. [CrossRef]
24. Kulal, P.M.; Dubal, D.P.; Lokhande, C.D.; Fulari, V.J. Chemical Synthesis of Fe$_2$O$_3$ Thin Films for Supercapacitor Application. *J. Alloys Compd.* **2011**, *509*, 2567–2571. [CrossRef]
25. Onofre, Y.J.; Catto, A.C.; Bernardini, S.; Fiorido, T.; Aguir, K.; Longo, E.; Mastelaro, V.R.; da Silva, L.F.; de Godoy, M.P.F. Highly Selective Ozone Gas Sensor Based on Nanocrystalline Zn$_{0.95}$Co$_{0.05}$O Thin Film Obtained Via Spray Pyrolysis Technique. *Appl. Surf. Sci.* **2019**, *478*, 347–354. [CrossRef]
26. Ardekani, S.R.; Aghdam, A.S.R.; Nazari, M.; Bayat, A.; Yazdani, E.; Saievar-Iranizad, E. A Comprehensive Review on Ultrasonic Spray Pyrolysis Technique: Mechanism, Main Parameters and Applications in Condensed Matter. *J. Anal. Appl. Pyrolysis* **2019**, *141*, 104631. [CrossRef]

27. Kamoun, O.; Mami, A.; Amara, M.A.; Vidu, R.; Amlouk, M. Nanostructured Fe, Co-Codoped MoO$_3$ Thin Films. *Micromachines* **2019**, *10*, 138. [CrossRef]

28. Ayed, R.B.; Ajili, M.; Thamri, A.; Kamoun, N.T.; Abdelghani, A. Substrate Temperature Effect on the Crystal Growth and Optoelectronic Properties of Sprayed α-Fe$_2$O$_3$ Thin Films: Application to Gas Sensor and Novel Photovoltaic Solar Cell Structure. *Mater. Technol.* **2018**, *33*, 769–783. [CrossRef]

29. Fareed, S.S.; Mythili, N.; Vijayaprasath, G.; Chandramohan, R.; Ravi, G. A-Fe$_2$O$_3$ Nanoparticles as a Byproduct from the Thin Film (Silar) Deposition Process: A Study on the Product. *Mater. Today Proc.* **2018**, *5*, 20955–20965. [CrossRef]

30. Mia, M.N.H.; Pervez, M.F.; Hossain, M.K.; Rahman, M.R.; Uddin, M.J.; Al Mashud, M.A.; Ghosh, H.K.; Hoq, M. Influence of MG Content on Tailoring Optical Bandgap of MG-Doped ZnO Thin Film Prepared by Sol-Gel Method. *Results Phys.* **2017**, *7*, 2683–2691. [CrossRef]

31. Reveendran, R.; Khadar, M.A. Structural, Optical and Electrical Properties of Cu Doped α-Fe$_2$O$_3$ Nanoparticles. *Mater. Chem. Phys.* **2018**, *219*, 142–154. [CrossRef]

32. Juwhari, H.K.; Ikhmayies, S.J.; Lahlouh, B. Room Temperature Photoluminescence of Spray-Deposited ZnO Thin Films on Glass Substrates. *Int. J. Hydrogen Energy* **2017**, *42*, 17741–17747. [CrossRef]

33. Makuku, O.; Mbaiwa, F.; Sathiaraj, T.S. Structural, Optical and Electrical Properties of Low Temperature Grown Undoped and (Al, Ga) Co-doped ZnO Thin Films by Spray Pyrolysis. *Ceram. Int.* **2016**, *42*, 14581–14586. [CrossRef]

34. Srinatha, N.; Raghu, P.; Mahesh, H.M.; Angadi, B. Spin-Coated Al-Doped ZnO Thin Films for Optical Applications: Structural, Micro-Structural, Optical and Luminescence Studies. *J. Alloys Compd.* **2017**, *722*, 888–895. [CrossRef]

35. Goncalves, L.F.; Rocha, L.S.R.; Longo, E.; Simões, A.Z. Calcium Doped BiFeO$_3$ Films: Rietveld Analysis and Piezoelectric Properties. *J. Mater. Sci. Mater. Electron.* **2018**, *29*, 784–793. [CrossRef]

36. Fouad, O.A.; Ismail, A.A.; Zaki, Z.I.; Mohamed, R.M. Zinc Oxide Thin Films Prepared by Thermal Evaporation Deposition and Its Photocatalytic Activity. *Appl. Catal. B Environ.* **2006**, *62*, 144–149. [CrossRef]